Micromachined Infrared Thermopile Detector Based on a Suspended Film Structure

Cheng LEI[1†*], Yihao GUAN[1,2†], Ting LIANG[1], Xuezhan WU[1], Yuehang BAI[1], Mingfeng GONG[1], Pingang JIA[1], and Jijun XIONG[1]

[1] *The State Key Laboratory of Dynamic Measurement Technology, North University of China, Taiyuan 030051, China*

[2] *Integrated Circuit Business Group, China Resources Microelectronics Limited, Wuxi 21400,China*

[*]Corresponding author: Cheng LEI E-mail: leicheng@nuc.edu.cn

[†]These authors contributed equally to this work and should be considered co-first authors

Abstract: The micro-electromechanical system (MEMS) infrared thermopile is the core working device of modern information detection systems such as spectrometers, gas sensors, and remote temperature sensors. We presented two different structures of MEMS infrared thermopiles based on suspended film structures. They both deposited silicon nitride over the entire surface as a passivated absorber layer in place of a separate absorber zone, and the thermocouple strip was oriented in the same direction as the temperature gradient. The same MEMS preparation process was used and finally two different structures of the thermopile were characterized separately for testing to verify the impact of our design on the detector. The test results show that the circular and double-ended symmetrical thermopile detectors have responsivities of 27.932 V/W and 23.205 V/W, specific detectivities of 12.1×10^7 cm·Hz$^{1/2}$·W^{-1} and 10.1×10^7 cm·Hz$^{1/2}$·W^{-1}, and response time of 26.2 ms and 27.06 ms, respectively. In addition, rectangular double-ended symmetric thermopile has a larger field of view than a circular thermopile detector, but is not as mechanically stable as a circular thermopile.

Keywords: Adiabatic groove; circular arrangement; double-ended symmetrical arrangement; thermopile; temperature gradient

Citation: Cheng LEI, Yihao GUAN, Ting LIANG, Xuezhan WU, Yuehang BAI, Mingfeng GONG, *et al.*, "Micromachined Infrared Thermopile Detector Based on a Suspended Film Structure," *Photonic Sensors*, 2023, 13(3): 230309.

1. Introduction

Any object above absolute zero emits radiation to the outside environment. The micro-electromechanical system (MEMS) infrared thermopile detector converts the received external radiation signal into temperature and converts the temperature into an electrical signal inside the detector, thus enabling non-contact measurement of temperature [1]. In addition to this, the detection of environmental gases can be achieved through the absorption of specific frequencies of infrared radiation (IR) by different gas components, even in arrays for the purpose of area imaging. The advantages are that they operate at room temperature, do not require chopping and bias voltages, have a wide spectral response range, and are simple and convenient to operate [2], which has led to the widespread study and application of infrared thermopile detectors.

The thermopile detector is mainly composed of absorber zone, thermocouple zone, support layer, and silicon substrate [3]. According to the Seebeck effect, the potential output of thermopiles is

Received: 24 October 2022 / Revised: 31 January 2023

DOI: 10.1007/s13320-023-0682-0
Article type: Regular

proportional to the temperature difference, so one of the ways to pursue high output performance of thermopiles is to increase the temperature difference and improve the output. Zhou *et al*. [4] designed and investigated a thermopile detector with thermocouples distributed in a microbridge. The thermopile detector consisted of 16 pairs of n-poly-Si/poly-Si thermocouples, which was fabricated by using a low-cost and high-yield complementary metal oxide semiconductor (CMOS) process. The microbridge-based thermopile device can achieve a 13.8% increase in output voltage compared with a thermopile device using a continuous film [4]. Zhang *et al*. [5, 6] designed a MEMS thermopile infrared detector with a high absorption-thermal conductivity film structure. The design of the thermal conductivity structure introduced low thermally conductive insulating silicon nitride material into the hot end, reducing the intermediate process of heat transfer and improving the performance, while further improving the detector performance by 20% by integrating a nano-forest structure. Shen *et al*. [7] designed an umbrella structured absorber embedded in the overhanging beam of the thermocouple by a strut, which achieved a better heat flow path and increased the temperature difference between the hot and cold junction. Ashraf *et al*. [8] improved the performance by integrating SU-8 into the absorber structure of the thermopile detector, resulting in improved absorption rates and enhanced hot end temperatures. In addition, there are many scholars who have achieved performance enhancement of thermopiles through process control. Zhou *et al*. [9] who achieved good resistance uniformity of polysilicon thermocouple strips by comparing reactive ion etching of undoped and heavily doped polysilicon based on hydrogen bromide (HBr) plasma. Li *et al*. [10] fabricated broadband absorbers consisting of quasi-ordered nanoforests and metal nanoparticles on a thermopile by using a plasma bombardment process, and tests showed that the photoinduced voltage of the devices showed a large increment of 433% at 100 $mW \cdot cm^{-2}$ light power density, in comparison with a contrast pristine thermopile. However, these infrared thermopile detectors are relatively complex to design and process. It has improved performance but is generally more costly. Silicon nitride is generally used as a passivation and absorption material because of its infrared absorption effect and narrow absorption range [11].

In this work, two different structures of MEMS infrared thermopile detectors were designed, fabricated, and tested based on a suspended film structure. The mechanical stability, responsivity, detection rate, response time, and field of view of the two thermopile detectors were compared and validated by simulating and testing to characterize the key points of our design. In Section 2, the relevant operating principles and performance parameters of the thermopiles are presented. Section 3 describes the design of two different structures of micromechanical infrared thermopile detectors. The MEMS fabrication process for the involved thermopile detectors is described in Section 4. The two different structures of the designed and prepared thermopile detectors are characterized by testing and discussed in detail in Section 5. Finally, Section 6 concludes the work in this paper.

2. Working principle

In this paper, two structures of thermopiles are proposed in order to compare the performance of the thermopiles and to better validate our design. When external infrared radiation is directed to the surface of the thermopile chip through the filter, the infrared absorber layer on the surface absorbs the radiation energy and converts the energy into heat, so that the temperature difference T_{diff} between the center and the edge of the suspended film is formed due to heat conduction. The temperature difference causes the carriers in the thermocouple strip to move directionally and gather at the cold end, resulting in a temperature difference electric potential U, according to the Seebeck effect. It is generally expressed as [3]

$$U = NT_{\text{diff}}\alpha_{a-b} \tag{1}$$

where N is the number of thermocouple pairs in the thermopile, T_{diff} is the average temperature difference from the hot end to the cold end of the thermocouple strip, and α_{a-b} is the difference in Seebeck coefficients between thermocouple strips of two different materials. According to the voltage output equation, increasing the temperature difference can effectively improve the voltage response.

The performance of a thermopile is generally characterized by the detector's responsivity, specific detectivity, response time, and thermopile resistance. Of these, the responsivity is generally characterized by the ratio of response voltage to IR radiated power, which is expressed as [12, 13]

$$R_v = \frac{U}{P_0} = \frac{U}{\varphi_0 A_d} \tag{2}$$

where P_0 is the IR radiated power and A_d is the area of the absorption zone of the device, as we have designed to deposit silicon nitride over the entire surface as a passivated absorption layer, our absorption zone area is equivalent to the cavity area. φ_0 is the radiant power density at the surface of the absorption zone of the device, and φ_0 is also generally expressed as [14]

$$\varphi_0 = \frac{C_r \sigma \varepsilon_1 \left(T_1^4 - T_0^4\right) A_s}{\pi d_0^2} \tag{3}$$

where C_r is the root mean square conversion factor, σ is the Stephen Boltzmann constant, ε_1 is the emissivity of the blackbody, A_s is generally the area of the blackbody, d_0 is the distance from the blackbody to the detector surface, T_1 is the blackbody temperature, and T_0 is the ambient temperature.

The specific detectivity, which can indicate the detector's detection capability, is generally expressed by the formula [1]:

$$D^* = \frac{R_v \sqrt{A_d \Delta f}}{U_n} \tag{4}$$

where Δf is the test bandwidth, generally taken as 1 Hz, and U_n is the noise voltage of the thermopile detector, which can be expressed as[2]

$$U_n = \sqrt{4kR_0 T_0 \Delta f}\ . \tag{5}$$

The response time of the thermopile is also important and is mainly related to the heat capacity C_{th} and thermal conductivity G_{th} of the thermocouple, mainly expressed as [15]

$$\tau = \frac{C_{\text{th}}}{G_{\text{th}}}\ . \tag{6}$$

In addition to this, the thermopile resistance is an important reference criterion for our design, our back-end micro-controller unit (MCU) requires less than 198 kΩ to be sufficient. The resistance of the thermopile consists of the sum of the resistance of all thermocouple strips of two different materials. As we use P-type polycrystalline silicon and aluminium for the thermocouple strip, the thermopile resistance is mainly determined by the P-type polycrystalline silicon thermocouple strip. Thermopile resistance is generally expressed as [16]

$$R_0 = N\sum_{i=1}^{2} \gamma_i \frac{l_i}{d_i w_i} \tag{7}$$

where γ_i is the resistivity of the thermocouple strip, and l_i ,d_i, and w_i are the length, height, and width of the thermocouple strip, respectively.

3. Structure design

Based on the Seebeck effect, we have designed two thermopile structures, as shown in Fig. 1, a circular thermopile and a double-ended symmetrical rectangular thermopile, respectively. The main design elements of the designed thermopiles, although different in structure, are essentially the same. The detailed information for theory analysis and design can be found in our previous reports [17, 18].

(1) Using a supporting membrane structure.

(2) Using the same thermocouple material.

(3) Eliminating separate absorption zones and depositing silicon nitride as a passivated absorption layer on the entire device surface.

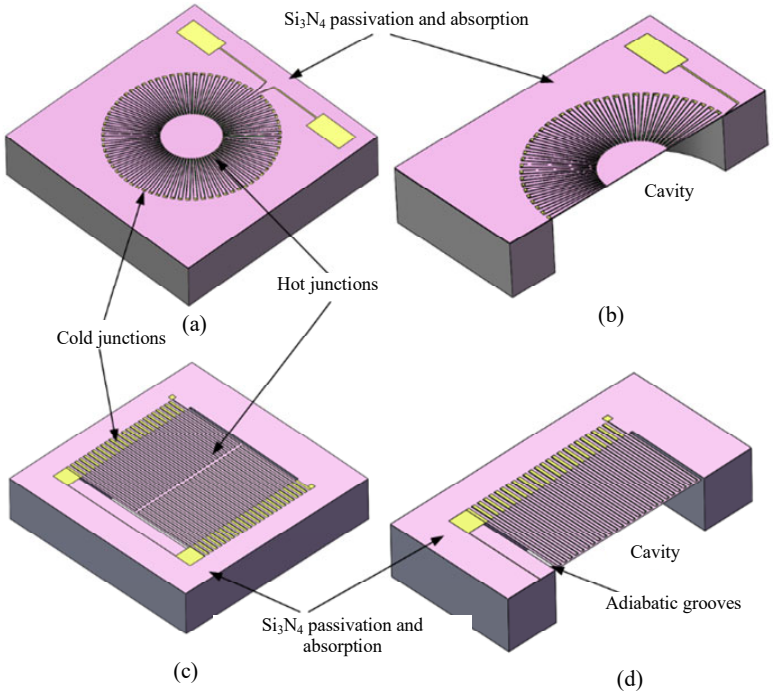

Fig. 1 Schematic diagram of the thermopile structure designed in this paper: (a) circular thermopile, (b) section of the circular thermopile, (c) rectangular double-ended thermopile, and (d) section of the rectangular double-ended thermopile.

(4) Thermocouple strips as parallel to the temperature gradient as possible and orthogonal to the isotherm.

(5) The chips are of the same size.

The response voltage of the thermopile is related to the difference in the Seebeck coefficient of the material. The material of the thermopile was therefore composed of P-polySi and Al, which guaranteed a reliable difference in the Seebeck coefficient and a certain degree of cost saving. A series of designs were developed for the double-ended symmetrical rectangular thermopile. In order to increase the duty cycle of the square chip, the thermocouple strip was arranged in a double-ended symmetrical arrangement; the hot end of the thermocouple strip was extended towards the center to the very center of the diaphragm; in order to keep the thermocouple strip parallel to the temperature gradient, we opened adiabatic grooves on both sides of the edge parallel to the thermocouple strip, and the adiabatic groove was kept parallel to the thermocouple strip, thus keeping the thermocouple strip parallel to the temperature gradient, and its temperature distribution cloud is shown in Fig. 2.

We have therefore determined the basic dimensions of the two thermopile configurations through finite element thermoelectric coupling simulation optimization, as shown in Table 1.

Table 1 Structural parameters of the thermopile designed in this paper.

Parameter	Unit	Circular thermopile	Rectangular thermopile
Chip	μm	1 800×1 800×0.4	1 800×1 800×0.4
Absorption area/cavity	μm	Φ=1 200	1 100×1 100 (L×W)
P-ploySi	μm	690×4×0.8	690×5×0.8
Al	μm	400×3×0.4	400×3×0.4
Support layer 1 (SiO_3)	μm	1 800×1 800×1.6	1 800×1 800×1.6
Support layer 2 (Si_3N_4)	μm	1 800×1 800×0.55	1 800×1 800×0.55
Passivation layer (Si_3N_4)	μm	1 800×1 800×0.2	1 800×1 800×0.2
Logarithm of thermocouple bar	/	72	50
Resistance	kΩ	144.036	138.575

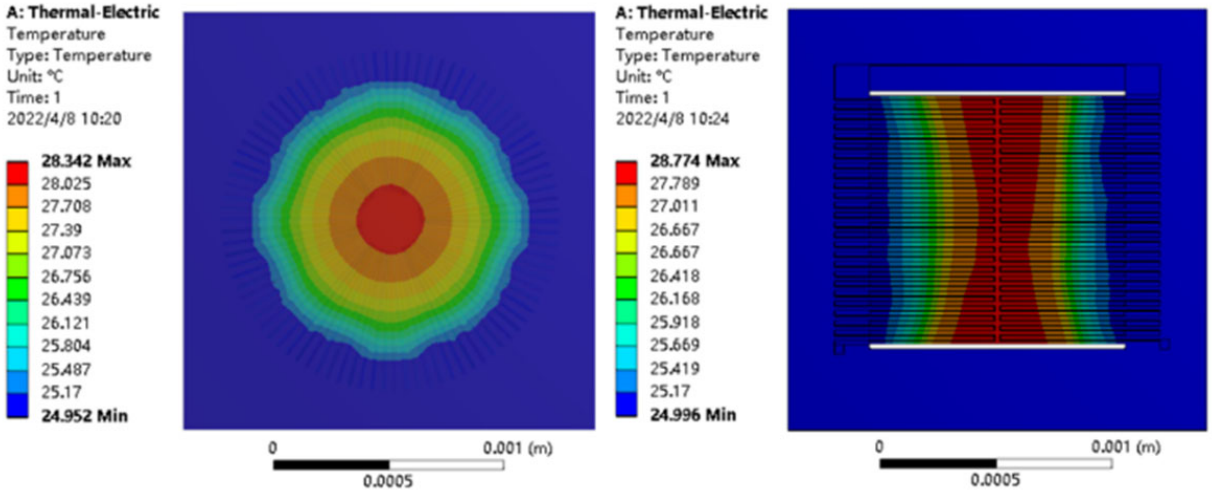

(a) (b)

Fig. 2 Temperature distribution clouds for two structures of thermopiles: (a) circular thermopile temperature distribution clouds and (b) rectangular double-ended thermopile temperature distribution clouds.

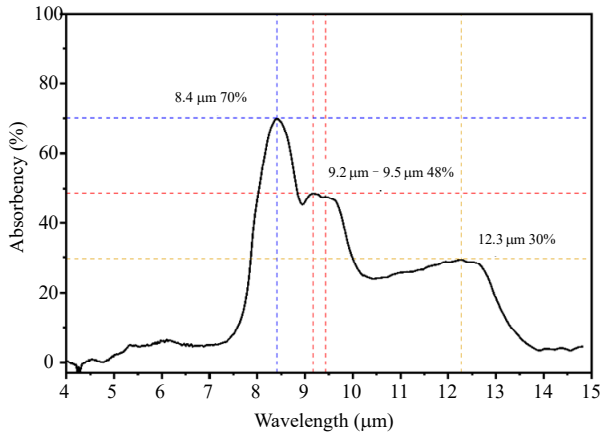

Fig. 3 Infrared absorption spectra of SiO_2-Si_3N_4-Si_3N_4 composite film layers.

Our support films were made of silicon oxide prepared by thermal oxidation and silicon nitride prepared by low pressure chemical vapor deposition (LPCVD), with a layer of silicon nitride deposited by plasma enhanced chemical vapor deposition (PECVD) as a passivation layer and IR absorber layer on the most surface after the preparation of the thermocouple strip. In order to test the infrared optical properties of our composite film layers, the composite suspended film layers of the prepared thermopiles were film released and tested by a Fourier infrared spectroscopy (FT-IR) tester. We tested the transmittance and reflectance of the composite film layers separately and processed to obtain the infrared absorption spectra of the composite film layers. Figure 3 shows the IR absorbance of the prepared composite film layer in the wavelength range of 4 μm – 15 μm. The results show that there is an absorption peak at 8.4 μm with an absorbance of up to 70%; there is also good absorption at 9.2 μm – 9.5 μm with 48%; the absorption in the band of 10 μm – 12.5 μm is also around 30%.

4. Preparation of devices

The two different structures of the thermopiles designed in this paper were prepared using standard MEMS processes and both structures were performed on the same wafer, with the exception of the double-ended symmetric thermopile which required a separate etching process due to the presence of its adiabatic grooves. The main process flow for the preparation of the thermopile detector is shown in Fig. 4.

Firstly, as shown in Fig. 4(a), we prepared silicon oxide 1.6 μm on the wafer surface sequentially by thermal oxidation process, and deposited silicon nitride 550 nm by LPCVD as a composite support film layer for the thermopile, followed by deposition of polysilicon $8\,000\times10^{-10}$ m by LPCVD as the

thermocouple strip material; before patterning, the polysilicon film layer was ion implanted with a doping dose of $1\times10^{16}\,cm^{-2}$ and annealed to form P-polySi. The next step is to prepare the surface structure of the thermopile as shown in Figs. 4(b) – 4(e), which mainly consists of poly-silicon thermocouple strips prepared by patterning, aluminium thermocouple strips prepared by sputter stripping, and alloy annealed to form ohmic contacts; passivation materials are required to avoid oxidation of the thermocouple strip structure when directly exposed to air, which affects device performance and lifetime.

Silicon nitride has both better IR absorption and passivation protection, compared with silicon oxide. A 2000×10^{-10} m silicon nitride was then prepared on the surface using a PECVD process and etched to expose the pads. No separate design was required to prepare the absorption zone and the entire passivated layer of silicon nitride absorbs external radiation. Most importantly, the adiabatic grooves of the double-ended symmetrical rectangular thermopile were prepared as shown in Fig. 4(f), where only two grooves parallel to the direction of the thermocouple strip were etched on both sides of the square double-ended symmetrical thermopile perpendicular to the thermocouple strip to slow or even stop the central temperature increment towards the perpendicular thermocouple strip, while the circular structure as a whole was protected by the photoresist. Finally, the thermopile structure was released by deep reactive ion etching (DRIE) from the back side, as shown in Fig. 4(g).

The two different structures of thermopile infrared detectors designed in this paper have been successfully prepared and their scanning electron microscope (SEM) images are shown in Fig. 5. The size of the prepared detector chips are both $1.8\times1.8\,mm^2$, where Fig. 5(a) shows a double-ended symmetric square thermopile chip, Fig. 5(b) shows the adiabatic slot of a double-ended symmetric square thermopile, Fig. 5(c) shows a circular thermopile chip, and Fig. 5(d) shows the hot end arrangement of a circular thermopile.

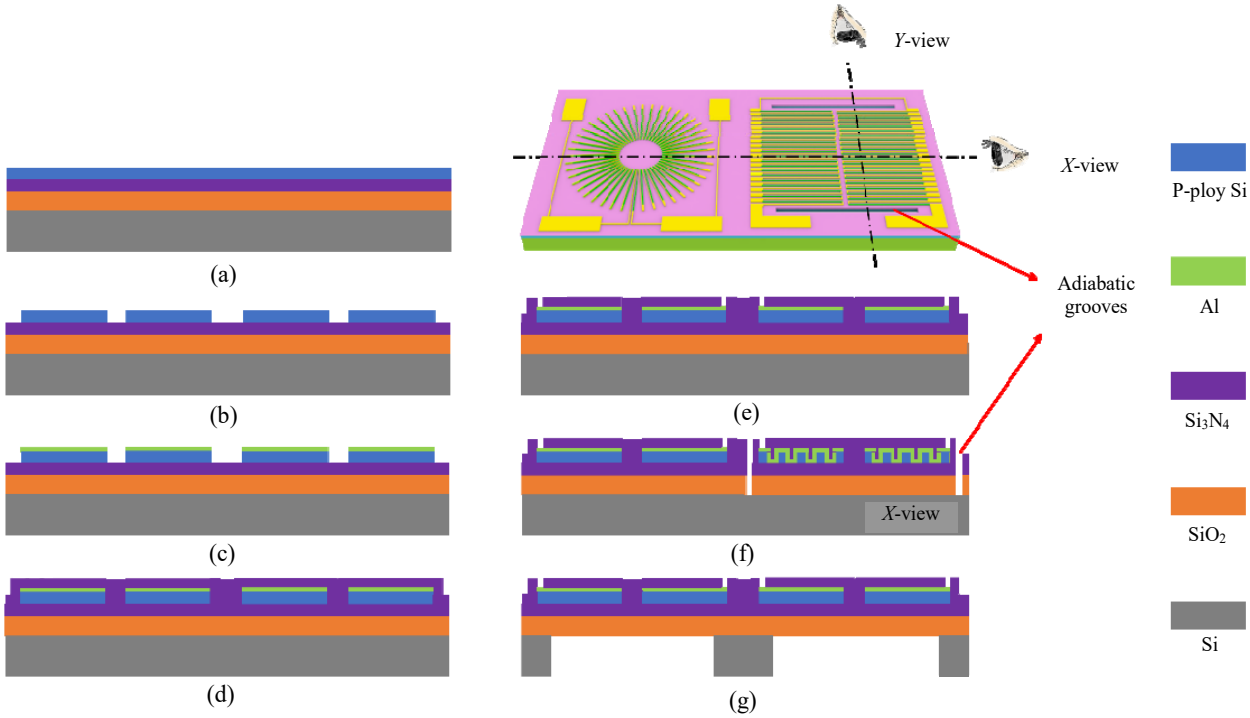

Fig. 4 MEMS infrared thermopile key preparation process: (a) preparation of composite support film layer and polysilicon, (b) etching to obtain polysilicon thermocouple strips, (c) deposition of metallic aluminum and etching to obtain aluminum thermocouple strips, (d) deposition of silicon nitride film layer for passivation absorption layer, (e) etching to expose the pads, (f) etching to prepare the adiabatic groove, and (h) deep silicon etching to release the film.

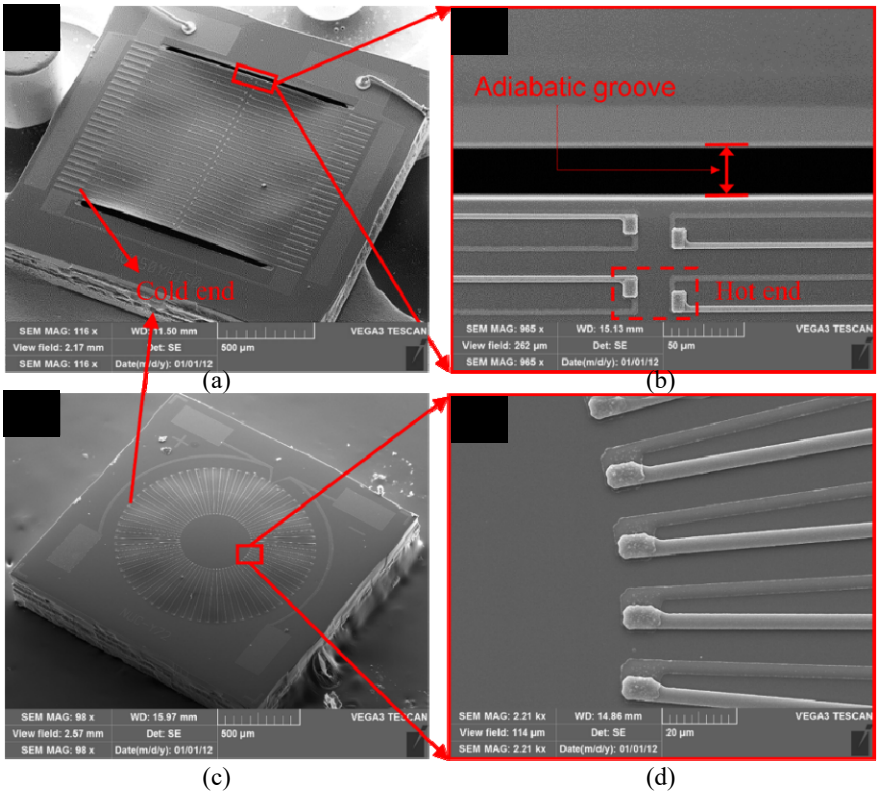

Fig. 5 Designed thermopile SEM image: (a) double-ended symmetrical rectangular thermopile, (b) adiabatic groove of double-ended symmetrical rectangular thermopile, (c) circular thermopile, and (d) layout of the hot end of the circular thermopile.

To improve the performance of the double-ended symmetrical thermopile, we prepared adiabatic grooves on both edges perpendicular to the thermocouple strip direction, where the adiabatic grooves were kept parallel to the thermocouple strip, so that the membrane structure of the square thermopile was not a closed membrane. In order to assess the mechanical stability of both structures, stress analysis and displacement analysis were carried out by means of ANSYS finite element simulations. By adding fixed constraints to the structural substrate and applying an acceleration of 10 000 g in the *Y*-axis direction, the simulation results are shown in Fig. 7, where Figs. 7(a) and 7(c) are the displacement distribution clouds of the device, and Figs. 7(b) and 7(d) are the stress distribution clouds of the device. Figures 7(a) and 7(c) show that the maximum displacements of the circular thermopile and the double-ended symmetric rectangular thermopile are 0.000 57 μm and 0.000 73 μm, respectively. As can be seen from Figs. 7(a) and 7(d), the stresses in the circular membrane structure were mainly distributed around the perimeter, while the stresses in the rectangular membrane structure with adiabatic grooves were mainly distributed near the cold end of the adiabatic grooves, and the maximum concentrated stress in the rectangular structure with adiabatic grooves (0.512 MPa) was double the maximum concentrated stress in the circular structure (0.262 MPa). A double-ended symmetrical rectangular thermoelectric stack with adiabatic grooves failed as shown in Fig. 8, with a ruptured surface near the cold end of the adiabatic grooves, causing the surface thermocouple strip to break, which corresponds to the results of our simulations. Thus, a circular thermopile has greater mechanical stability than a double-ended symmetrical rectangular thermopile.

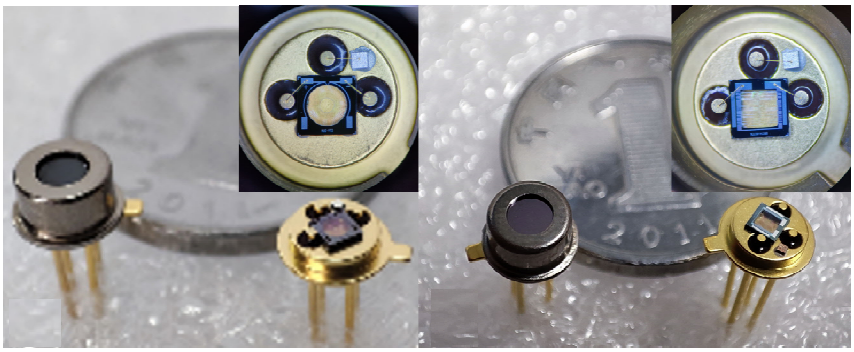

(a) (b)

Fig. 6 Thermopile infrared detector with TO package: (a) circular thermopile and (b) double-ended symmetrical rectangular thermopile.

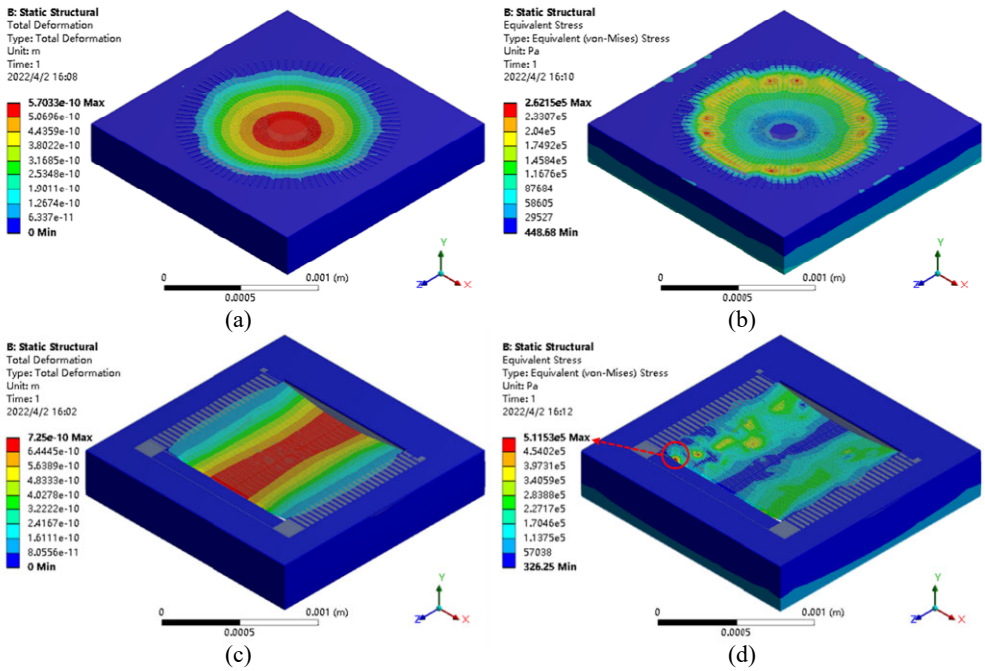

(a) (b)

(c) (d)

Fig. 7 ANSYS finite element simulation of the circular thermopile and the double-ended symmetrical rectangular thermopile: (a) the simulated deformation shape of the circular thermopile, (b) the simulated stress intensity of the circular thermopile, (c) the simulated deformation shape of the double-ended symmetrical rectangular thermopile, and (d) the simulated stress intensity of the double-ended symmetrical rectangular thermopile.

5. Testing and discussion

In order to better determine the electrical properties of the designed and prepared thermopiles, we used the same TO-46 package for both structures and characterized them using the same test protocol as shown in Fig. 6. The test equipment mainly used a blackbody, chopper, chopper console and lock-in amplifier. The thermopile infrared detector in TO vacuum package was placed at a position 12 cm from the blackbody radiation source, the chopper was placed between the blackbody and the detector, the detector output was connected to a lock-in amplifier, and the chopper frequency was used as the reference frequency of the lock-in amplifier for phase locking, and data acquisition was performed via the LABVIEW console.

The relationship between current and voltage was first tested by applying a voltage across the electrodes of the device using a semiconductor analyser. The *I-V* characteristic curves are shown in Fig. 9. The results showed that the difference in

resistance values between the circular and double-ended symmetrical rectangular thermopile devices was not significant, fell within the range of process redundancy, and was relatively close to the theoretical design value.

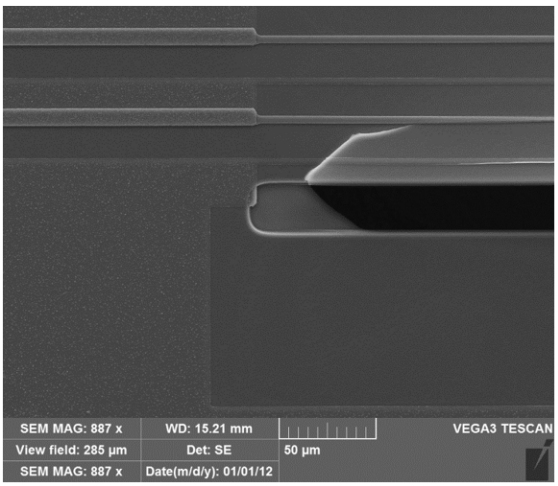

Fig. 8 SEM image of a failed double-ended symmetrical square thermopile structure with adiabatic grooves, with a broken diaphragm near the cold end.

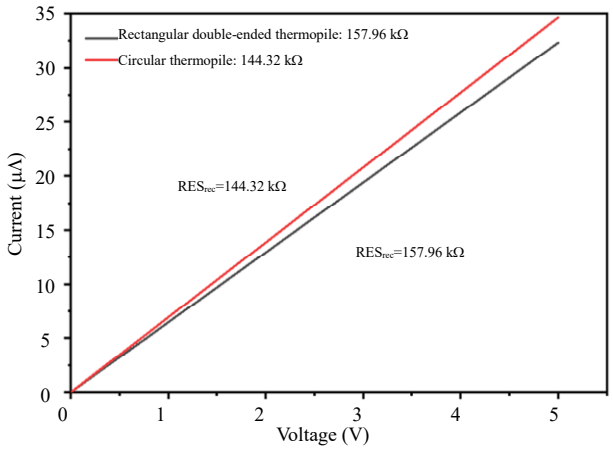

Fig. 9 *I-V* characteristic curves for two different structures of thermopiles.

In the testing process, as shown in Fig. 10, we first set the blackbody radiation temperature to 500 K and the detector substrate temperature to the same room temperature. The detector surface was 12 cm away from the blackbody radiation surface and the chopper was located between the blackbody and the detector, by adjusting the chopper frequency so that the radiation period on the detector surface changed, thus producing an output square wave. To reduce the effect of the Gaussian plane of the radiation source on the test results, the chopper blade should be as close as possible to the detector surface and the detector should be located in the center of the radiation surface.

Figure 11 shows the output waveforms of the two structures at 5 Hz with a 500 K radiation source. The test results show that the voltage amplitudes of the double-ended symmetrical rectangular structure and the circular structure after the phase-locked amplifier are 10.41 mV and 14.83 mV, respectively. Figure 11(b) shows the rising edge of the thermopile waveforms of the two structures in Fig. 11(a). The results show that the response time is 27.06 ms and 26.2 ms, respectively, and the output of the double-ended symmetrical thermopile is still different from that of the circular arrangement although it is optimized by adiabatic groove.

The existence of chopper makes thermopile voltage response low. In order to avoid interference with device performance testing from choppers and the surrounding environmental radiation and convection, we fixed the infrared thermopile detector on a special test substrate, and the distance between the detector and the blackbody radiation surface was reduced to 30 mm, and the detector was in a confined space during the test, without adding a chopper, and the voltage output of each device was read directly through a high-precision multimeter measurement at this time.

Finally, the voltage value read at this time was used to further characterize the responsivity, specific detectivity, and other performance. Table 2 summarizes the performance parameters of the two thermopile detectors. The responsivity and specific detectivity were measured in a static test in a 30 mm confined space, and the time constant was determined by the time required for output to reach 63% of the maximum value at a 5 Hz chopper frequency.

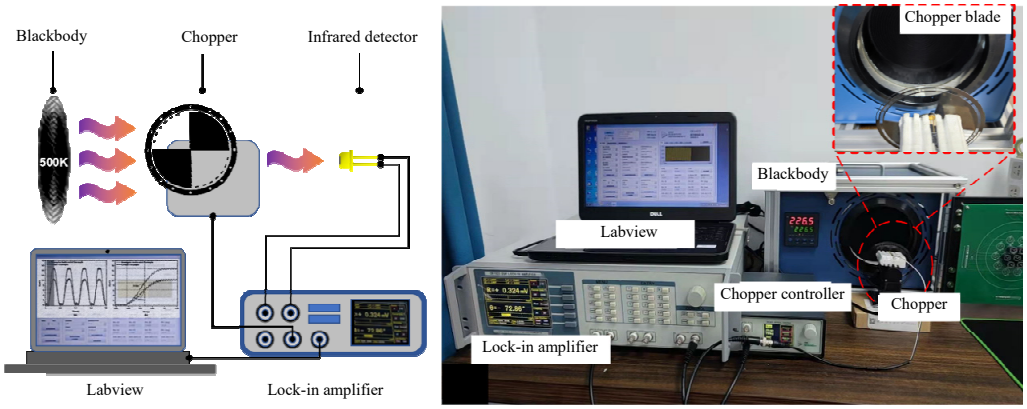

(a) (b)

Fig. 10 Infrared test system: (a) infrared test system schematic and (b) infrared test system physical diagram.

Table 2 Performance parameters of circular thermopile and double-ended symmetrical rectangular thermopile.

Parameter	Test conditions	Unit	Circular thermopile	Rectangular thermopile
Electrical resistance	25 °C	kΩ	144.32	157.96
Response voltage	*D*: 30 mm	mV	15.518	12.892
Responsivity	*D*: 30 mm	V/W	27.932	23.205
Specific detectivity	500 K, 8 μm–14 μm, 4 Hz	10^7 cmHz$^{1/2}$W^{-1}	12.1	10.1
Noise voltage	/	nV/Hz$^{1/2}$	48.724	50.988
Temperature coefficient	/	%/k	0.031	0.024
Field of view	@50% target signal	°	87	90
Response voltage	D: 120 mm	mV	12.111	9.616
Response time	D: 120 mm, 5 Hz	ms	26.2	27.06

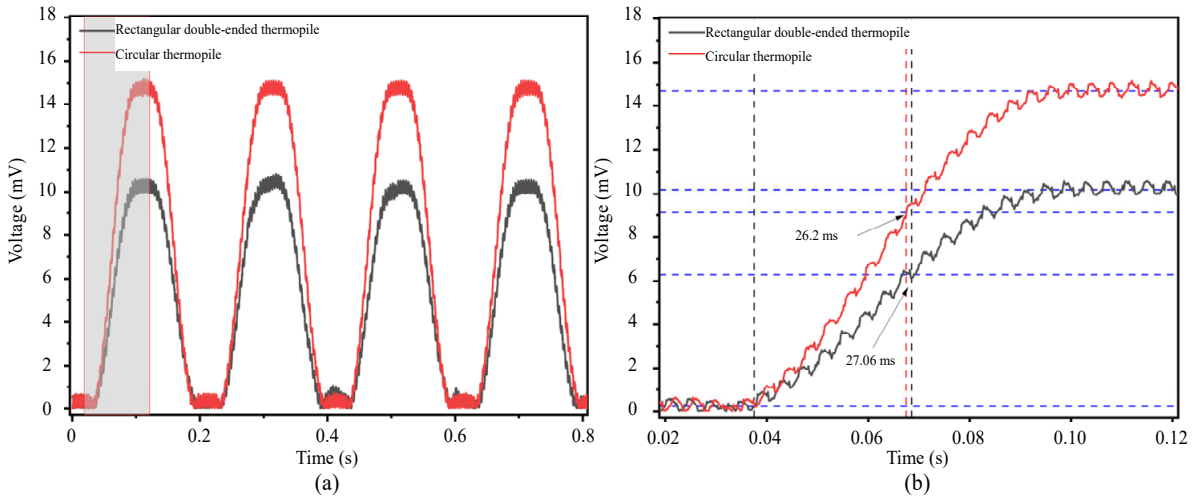

(a) (b)

Fig. 11 Results of thermopile test with symmetrical and circular structures: (a) waveforms of thermopile infrared detectors for two structures and (b) rising edges of thermopile detectors for two structures.

As shown in Table 2, the circular thermopile has higher responsivity and specific detectivity, and the response time is also smaller than that of the double-ended symmetrical thermopile with an adiabatic groove structure. This shows that the overall performance of the circular thermopile is better than that of the double-ended symmetrical thermopile with adiabatic groove structure.

The higher responsivity and specific detectivity of the circular thermopile is due to the higher

temperature utilization at the hot end, and it has a higher average temperature difference between the hot and cold ends. Although the rectangular thermopile has improved its performance to some extent by increasing the average temperature of the hot end through the adiabatic groove, in the actual test process, when the rectangular thermopile receives external radiation on the detector surface, in addition to heat transfer from the hot end to the cold end in the form of heat conduction along the parallel direction of the thermocouple strip, there is also thermal convection and heat loss due to radiation from the hot end of the diaphragm near the location of the adiabatic groove to the nearby heat sink, so the temperature gradient is still orthogonal to the thermocouple strip, limiting the voltage response to some extent. In addition, although the adiabatic groove makes the temperature decrease only in the direction of the thermocouple strip and the average temperature difference is larger, which improves the performance, it also makes the thermal resistance of the contact between the suspension film and the silicon substrate increase, the structural thermal conductivity decreases, the response time is inversely proportional to the thermal conductivity, and thus the response time is also larger.

Afterwards, we also carried out temperature response tests for both structures of the detector. We fixed the detector 30 mm in front of the blackbody radiation surface source and varied the temperature of the blackbody source in steps of 5 °C in the range of 0–120 °C. Their output voltage values were recorded directly by a high precision multimeter, the results of which are shown in Fig. 12.

Finally, we also tested the field of view of both configurations of the thermopile IR detector. By setting up the field of view test system as shown in the figure, the angle between the device and the radiation plane was changed by rotating the rotating table on which the thermopile device was mounted and the response voltage was recorded and normalized as shown in Fig. 13. The low duty cycle of the thermocouple strip allowed the hot end of the thermocouple strip to be extended further towards the center, which to some extent improved the temperature difference and response of the circular structure, which in turn improved the field of view of the device.

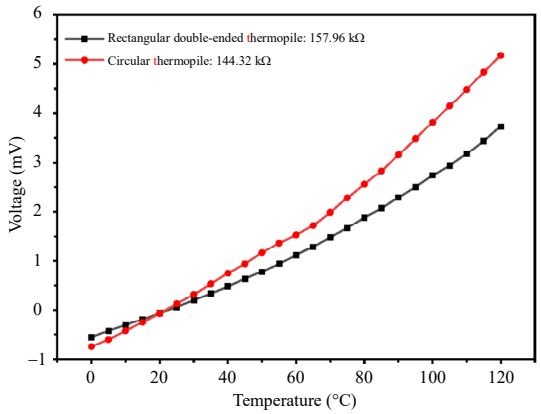

Fig. 12 Temperature response characteristics of the thermopile for two configurations.

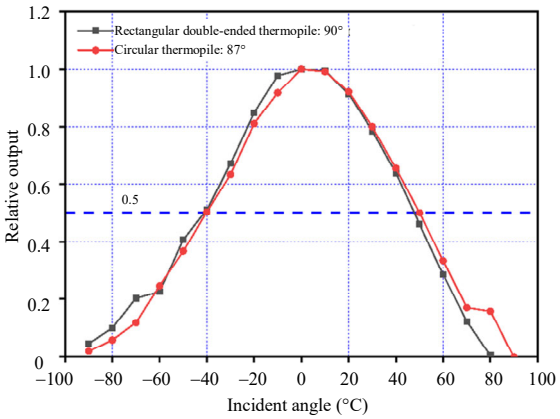

Fig. 13 Field of view of two structures of thermopiles.

6. Conclusions

This paper described the design, preparation, and testing of two different structures of infrared thermopile detectors. The two thermopiles maintained essentially the same design concept except for the different arrangements of the thermocouple strips, i.e., the silicon nitride was deposited on the entire surface as a passivated absorber layer. The thermal strips were kept parallel to the temperature gradient so that the temperature was transferred only in the direction of the thermal

strips towards the cold end, where the carrier motion was as consistent as possible with the temperature gradient. And the hot end was elongated as far as possible towards the center to maintain a higher temperature difference. Both thermopiles were prepared using the same standard MEMS process and finally the back side was dry etched with a deep silicon release suspension film to achieve thermopile thermal isolation. Finally, an infrared test system was set up for characterization, and the results showed that although the double-ended rectangular thermopile had a large increase in response voltage through the adiabatic groove, and the circular thermopile had a higher responsivity, higher specific detectivity, smaller response time, and better mechanical stability. However, the disadvantage of the circular thermopile is that the field of view is not as good as that of the rectangular double-ended thermopile.

Acknowledgment

The authors would like to appreciate Micro/Nano Fabrication Center, North University of China, for the supporting of MEMS chip manufacturing. They would also like to appreciate the Suzhou Institute of Nano-Tech and Nano-Bionics, CAS and Wuxi Hinovaic, for providing the tools in the processes.

This work was supported in part by the National Natural Science Foundation of China (Grant No. 51935011), Innovative Research Group Project of National Science Foundation of China (Grant No. 51821003), Fund for Shanxi "1331 Project" Key Subject Construction, Key Research and Development Project of Shanxi Province (Grant Nos. 202102030201001 and 202102030201009), and Key Special Project of Science and Technology of Shanxi Province (Grant No. 202201030201004).

References

[1] A. Graf, M. Arndt, and G. Gerlach, "Seebeck's effect in micromachined thermopiles for infrared detection," *A Review*, 2007, 13(4): 338–353.

[2] D. H. Xu, Y. L. Wang, B. Xiong, and T. Li, "MEMS-based thermoelectric infrared sensors: a review," *Frontiers of Mechanical Engineering*, 2017, 12 (4): 557–566.

[3] H. G. Hou, Q. Huang, G. Liu, and G. Qiao, "Enhanced performances of CMOS-MEMS thermopile infrared detectors using novel thin film stacks," *Infrared Physics and Technology*, 2019, 102: 103058.

[4] N. Zhou, X. Ding, H. Li, Y. Ni, Y. Pu, H. Mao, *et al.*, "A thermopile detector based on micro-bridges for heat transfer," *Micromachines*, 2021, 12 (12): 1554.

[5] C. Zhang, "Research on high absorption heat conduction MEMS thermopile infrared detector technology," Ph.D. dissertation, North University of China, 2021.

[6] C. Zhang, H. Mao, M. Shi, J. Xiong, K. Long, and D. Chen, "A fiber-Si_3N_4 composite nanoforest with high 7.6 to 11.6 um absorption for MEMS infrared sensors," in *Proceedings of the IEEE International Conference on Micro Electro Mechanical Systems (MEMS)*, Canada, 2020, pp. 949–952.

[7] T. W. Shen, K. C. Chang, C. M. Sun, and W. Fang, "Performance enhance of CMOS-MEMS thermoelectric infrared sensor by using sensing material and structure design," *Journal of Micromechanics and Microengineering*, 2019, 29(2): 025007.

[8] S. Ashraf, C. G. Mattsson, and G. Thungström, "Fabrication and characterization of a SU-8 epoxy membrane-based thermopile detector with an integrated multilayered absorber structure for the mid-IR region," *IEEE Sensors Journal*, 2019, 19(11): 4000–4007.

[9] N. Zhou, J. Li, H. Mao, H. Liu, J. Gao, J. Xiang, *et al.*, "The study of reactive ion etching of heavily doped polysilicon based on HBr/O_2/He Plasmas for thermopile devices," *Materials*, 2020, 13(19): 4278.

[10] M. Li, M. Shi, B. Wang, C. Zhang, S. Yang, Y. Yang, *et al.*, "Quasi-ordered nanoforests with hybrid plasmon resonances for broadband absorption and photodetection," *Advanced Functional Materials*, 2021, 31(38): 2102840.

[11] C. Lei, H. Y. Mao, W. Ou, C. Xue, L. Tang, T. Yang,

et al., “A CMOS-MEMS IR device based on double-layer thermocouples,” *Microsystem Technologies*, 2016, 22: 1163–1171.

[12] Z. Wang, V. Leonov, P. Fiorini, and C. Van Hoof, “Realization of a wearable miniaturized thermoelectric generator for human body applications,” *Sensors and Actuators A: Physical*, 2009, 156(1): 95–102.

[13] Y. Li, H. Zhou, T. Li, Y. Wang, Y. Liu, and Y. Wang, “CMOS-compatible 8×2 thermopile array,” *Sensors and Actuators A: Physical*, 2010, 161(1): 120–126.

[14] H. Zhou, P. Kropelnicki, J. M. Tsai, and C. Lee, “Development of a thermopile infrared sensor using stacked double polycrystalline silicon layers based on the CMOS process,” *Journal of Micromechanics and Microengineering*, 2013, 23(6): 065026.

[15] I. H. Choi and K. D. Wise, “A silicon-thermopile-based infrared sensing array for use in automated manufacturing,” *IEEE Transactions on Electron Devices*, 1986, 33(1): 72–79.

[16] C. Lei, “Key technology research on double-ended beam MEMS thermopile infrared detector,” Ph.D. dissertation, North University of China, 2016.

[17] T. Liang, Y. Guan, C. Lei, X. Wu, Y. Bai, J. Xiong, *et al.*, “Design and fabrication of a low-cost thermopile infrared detector,” *Micromachines*, 2021, 12(9): 1134.

[18] Y. Guan, C. Lei, T. Liang, Y. Bai, X. Wu, J. Xiong, *et al.*, “Design, preparation and characterization of a double-ended symmetric MEMS thermopile with adiabatic grooves,” *Infrared Physics & Technology*, 2022, 122: 104078.